



# Seismic numerical modelling of suspended piping trapeze restraint installations based on component testing

Daniele Perrone<sup>1</sup> · Emanuele Brunesi<sup>2</sup> · Andre Filiatrault<sup>1,3</sup> · Simone Peloso<sup>2</sup> · Roberto Nascimbene<sup>2</sup> · Clemens Beiter<sup>4</sup> · Roberto Piccinin<sup>4</sup>

Received: 18 September 2019 / Accepted: 21 March 2020 / Published online: 26 March 2020  
© Springer Nature B.V. 2020

## Abstract

The seismic performance of suspended piping systems can significantly compromise the functionality of critical facilities due to the incorporation of inadequate seismic design based on prescriptive empirical regulations and guidelines. The performance-based seismic design (PBSD) of non-structural elements requires the evaluation of performance parameters, based on experimental data or numerical studies, for comparison with engineering demand parameters. Few research studies available in the literature provide the performance parameters required to enable PBSD of piping systems and more specifically of suspended piping restraint installations. This paper discusses the numerical modelling of suspended piping trapeze restraint installations based on component testing. Reliable numerical models capable of predicting the force–displacement (backbone) curves of suspended piping restraint installations are developed based on monotonic and cyclic test data of the components that make up these installations. The prediction capabilities of the numerical models are assessed against the results of monotonic benchmark sub-assembly tests reported in a previous study. The numerical models developed in this study can be used to extract performance parameters from the predicted force–displacement curves to be used within a probabilistic PBSD framework without the need to conduct additional testing.

**Keywords** Non-structural elements · Suspended piping trapeze restraint installations · Numerical modelling · Performance-based seismic design

---

✉ Daniele Perrone  
daniele.perrone@iusspavia.it

<sup>1</sup> University School for Advanced Studies IUSS Pavia, Palazzo del Broletto – Piazza della Vittoria, Pavia, Italy

<sup>2</sup> European Centre for Training and Research in Earthquake Engineering, Pavia, Italy

<sup>3</sup> Department of Civil, Structural, and Environmental Engineering, State University of New York at Buffalo, Buffalo, USA

<sup>4</sup> Hilti Corporation, Schaan, Liechtenstein

## 1 Introduction

Recent advancements in earthquake engineering pointed out the importance of performance-based seismic design (PBSD). The concept of PBSD appeared for the first time in the Vision 2000 document prepared by the Structural Engineers Association of California (SEAOC 1995). Vision 2000 defines PBSD as a seismic design framework that couples desired system performance objectives with associated seismic hazard levels. In recent years, the PBSD methodology has been developed further through a rigorous probabilistic framework (Gunay and Mosalam 2013). Although PBSD has advanced substantially for some types of structural systems to the point where it is starting to be incorporated into building codes and standards (e.g. ASCE 2017), its application to non-structural building elements remains largely unexplored.

Recent earthquakes that have occurred worldwide have clearly demonstrated the poor seismic performance of non-structural elements (Filiatrault et al. 2001; Chock et al. 2006; Gupta and McDonald 2008; Ercolino et al. 2012; Miranda et al. 2012; Perrone et al. 2019). For example, piping systems that are key to the functionality of important facilities, such as hospitals and schools, suffered severe damage during recent earthquakes. Following the 2010 Chile earthquake, for example, the Santiago International Airport was closed for several days because of the severe damage to piping systems interacting with ceiling systems (Miranda et al. 2012). Similar inadequate performance of piping systems was also observed following the 2006 Hawaii Earthquake (Chock et al. 2006). The poor seismic performance of piping systems was generally due to the inadequate bracing of the pipes that led to excessive rotations of the piping joints (Tian et al. 2014).

The serviceability of a building is significantly affected by the damage to the multitude of typologies of non-structural elements. At the same time, non-structural elements represent most of the total investments in typical buildings and the economic losses ascribed to them are generally significantly higher than that of structural damage (O'Reilly et al. 2018). In the light of these considerations, the seismic behaviour of non-structural elements is now recognized to be a key issue in performance-based earthquake engineering.

In general, the poor seismic performance of non-structural elements can be associated to two main factors: (1) the empirical design prescriptions available in current seismic provisions and guidelines are generally inadequate and do not provide specific quantitative indications on how to achieve defined performance objectives within the PBSD framework and, (2) few experimental and numerical studies on the seismic performance of different typologies of non-structural elements are available in the public literature to clearly assess their performances under increasing seismic intensities.

The application of PBSD to non-structural elements requires on one hand the definition of performance objectives for each damage limit state through measurable engineering demand parameters and, on the other hand, the calibration of meaningful performance parameters characterizing the seismic response of non-structural elements (Filiatrault et al. 2018a). For example, the serviceability damage limit state of suspended piping systems could be related to the yielding of the trapeze restraint installations as well as to the leakage of the piping joints. This implies that the two performance parameters required to satisfy the serviceability limit state are the yield displacement of suspended piping trapeze restraint installations and the piping joint rotations at which significant leakage occurs. On the other hand, the ultimate limit state of suspended piping systems could be related to visible distortion or failure of components associated with measurable drop in load bearing capacity.

A reliable quantification of non-structural elements performance parameters for use in PBSD involves the development of detailed system design information by means of quasi-static cyclic tests and/or numerical analyses. The cyclic tests and the numerical analyses should be performed both at the component and system levels. Focusing on piping systems, quasi-static cyclic tests can provide data to define meaningful performance parameters of suspended piping trapeze restraint installations and piping joints, such as the initial stiffness, the yield and maximum strengths, the ultimate deformation and the displacement ductility capacity. Advanced nonlinear numerical models can then be used to predict the performance parameters for similar elements that have not been tested as well as to extend the analyses at the system level in order to quantify the system performance under prescribed building floor motions shaking.

The dynamic response of piping joints, mainly for fire sprinkler piping systems and medical gas pipelines, was investigated recently both from an experimental and numerical point of view (Tian et al. 2014, 2015a, b; Soroushian et al. 2015a, b; Blasi et al. 2018). These recent studies, however, did not address the dynamic response of suspended piping trapeze restraint installations. To the authors' knowledge, the only experimental data on the cyclic response of suspended piping trapeze restraint installations available in the public literature are those reported by Wood et al. (2014) and Perrone et al. (2020). Similarly, to the authors' knowledge, no numerical modelling of suspended piping trapeze restraint installations, both at the component and system levels has been reported in the public literature.

This paper discusses the numerical modelling of suspended piping trapeze restraint installations based on component testing. Reliable numerical models capable of predicting the force–displacement (backbone) curves of suspended piping trapeze restraint installations are developed based on monotonic and cyclic test data of the components that make up these installations. The prediction capabilities of the numerical models are assessed against the results of monotonic benchmark tests carried out previously on suspended piping trapeze restraint installation sub-assemblies (Perrone et al. 2020). These numerical models could then be used to predict the force–displacement curves of different suspended piping trapeze restraint installations in order to extract their performance parameters and predict their seismic response without the need to conduct additional sub-assembly testing.

## 2 Definition of trapeze restraint installations

The seismic restraint of suspended non-structural elements can be achieved through many available typologies of sway bracing systems. Seismic restraint installations are mainly used in critical facilities and industrial buildings due to the large number of piping systems, equipment and non-structural elements required for their continuous functionalities. Based on the typology of non-structural element to be restrained, seismic restraint can be achieved through wall and ceiling applications. A field survey carried out in industrial and commercial facilities in Italy indicated that the most used seismic restraint installations are ceiling applications made of channel frames and rod trapezes. Based on this information, four trapeze restraint installations were selected for this study (Fig. 1).

The first two seismic trapeze restraint installations consist of channel trapezes braced respectively in the transverse (Fig. 1a) and longitudinal (Fig. 1b) direction with respect to the pipes direction. The channel trapeze installation braced in the transverse direction is referred herein as “SS1”, while the channel trapeze braced in the longitudinal direction is

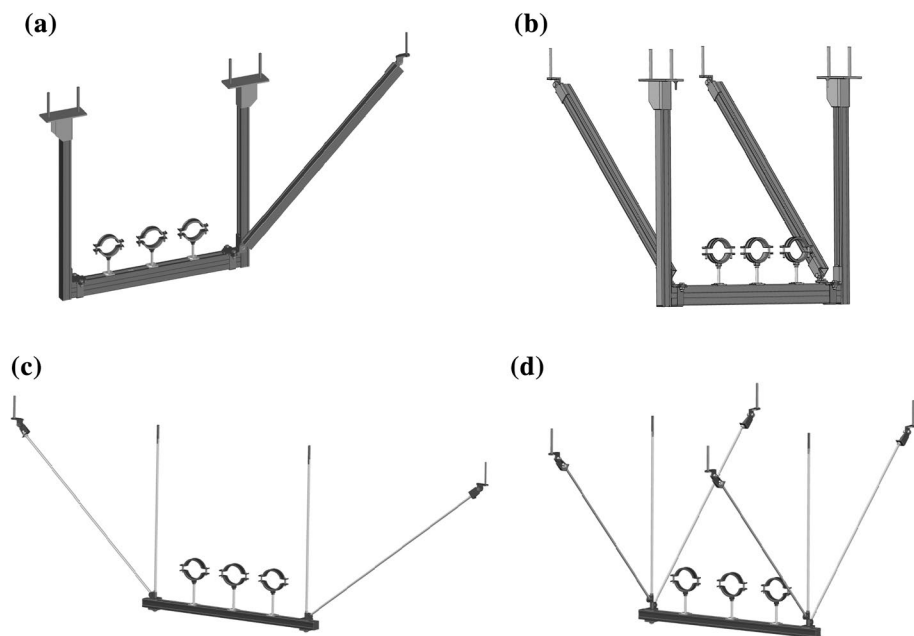


**Fig. 1** Suspended trapeze restraint installations: **a** Trapeze with transverse channel bracing system (SS1), **b** Trapeze with longitudinal channel bracing system (SS2), **c** Trapeze with transverse rod bracing system (SS3), **d** Trapeze with longitudinal rod bracing system (SS4)

referred as “SS2”. These two configurations typically include two vertical channels connected by a horizontal channel. Depending on the bracing direction, one or two diagonal elements are used to provide lateral restraint. The channels’ size is commonly equal to 41 mm square. The third and fourth typologies, referred herein as “SS3” and “SS4”, consist of trapeze assemblies with transverse (Fig. 1c) and longitudinal (Fig. 1d) rod bracing elements. Configuration “SS3” includes two 10-mm diameter threaded rods inclined at an angle of  $45^\circ$  from the vertical to provide the lateral bracing. Similar considerations in terms of inclination and diameter of the diagonal threaded rods apply to configuration “SS4”, but in this case four diagonal bracing rods are used. The connections between the steel channels and the threaded rods are guaranteed by hinges, while the connections between the vertical and diagonal elements and the supporting structure are provided by rail supports for the channel trapeze installations and by hinges for the rod trapeze installations. Finally, for all typologies, short threaded rods are connected to the horizontal channel through steel plates in order to connect the pipes to the trapeze installations. The pipes are secured in place by means of pipe rings bolted to the threaded rods. The dimensions and the inclination of the diagonal channels/rods vary with the applications. It is also possible to find some applications in which the transverse and longitudinal bracing elements are combined. Table 1 summarizes the main geometrical characteristics of the four suspended restraint trapeze installations considered in this study.

**Table 1** Main geometrical properties of suspended piping trapeze installations

ID	Frame typology	Bracing direction	Brace inclination (°)	Number of braces	Horizontal channel length (mm)	Height of vertical channels or rods (mm)
SS1	Channel	Transverse	45	1	800	800
SS2	Channel	Longitudinal	45	2	800	800
SS3	Rod	Transverse	45	3	900	600
SS4	Rod	Longitudinal	45	4	900	600

### 3 Sub-assembly benchmark tests

Perrone et al. (2020) carried out an extensive experimental program to investigate the global response of suspended piping restraint trapeze installations. These sub-assembly tests are used to benchmark the predictions of the numerical models developed in this work. The experimental program consisted of monotonic and cyclic tests carried out on an experimental set-up specifically designed to simulate real service conditions. During the tests, two suspended piping trapeze installations were loaded simultaneously (Fig. 2). The two trapeze installations were connected to each other through a system of four rigid steel pipes. The system of rigid pipes was used to realistically simulate gravity and seismic loading. The cyclic tests were carried out according to the FEMA 461 quasi static cyclic loading protocol (FEMA 2007). The FEMA 461 loading protocol is considered the most appropriate loading protocol available in the literature to perform cyclic tests on non-structural elements (Filiatrault et al. 2018b). The suspended piping trapeze installations exhibited a significant strength capacity and a ductile behaviour. No brittle failure occurred in any of the tests. The deformations were mainly concentrated in the components connecting the channel elements for configurations SS1 and SS2 (Fig. 3a), while the buckling of the diagonal and vertical rods (Fig. 3b) governed the response of the rod configurations SS3 and SS4. Further details regarding the observed behaviour and the performance parameters

**Fig. 2** General view of the experimental set-up

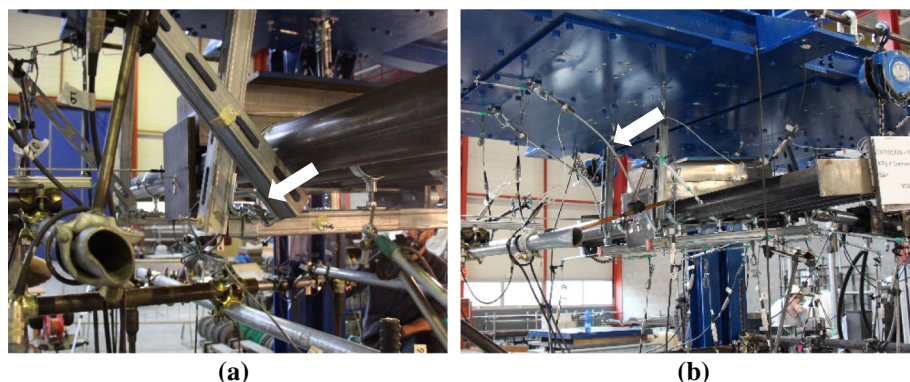


**Fig. 3** Damage observed during cyclic tests: **a** SS1 test specimen, **b** SS3 test specimen

extracted from the sub-assembly tests on the suspended piping trapeze installations considered in this study are reported in Perrone et al. (2020).

## 4 Component testing

### 4.1 Selection of critical components

An experimental program was carried out to evaluate the monotonic and cyclic response of the various components included in the four suspended trapeze piping installations described in the previous section. The observations made during the benchmark sub-assembly tests reported by Perrone et al. (2020) were used as a guide to identify the critical components to be tested. Figure 4 identifies those critical components for each trapeze configuration.

Six critical components were selected for testing based on a critical evaluation of the geometrical configuration of the suspended piping trapeze installations as well as on the results of the sub-assembly tests briefly described in the previous section. Table 2 lists and provides a short description of the components that were tested along with the indication of the suspended piping trapeze installations in which the components are included. Three components were tested for the two channel trapeze configurations: (1) the connection between the vertical channel and the supporting structure (referred as “C1”), (2) the connection between the horizontal and vertical channel (referred as “C2”), and (3) the rail support connecting the diagonal channel to the supporting structure (referred as “C3”). The results of the sub-assembly tests showed that the main deformations occurred in components C2 and C3. Component C1 was also tested because it affects the global stiffness of the channel trapeze installations. For the rod trapeze configurations, two components were tested: (1) the hinge connecting the diagonal rod to the supporting structure (referred as “C4”), and (2) the hinge connecting the diagonal and vertical rods (referred as “C5”). In the rod trapeze configurations, the vertical rods are bolted to the supporting structure or fixed through anchors, for this reason these connections were not tested during the experimental program. Finally, the pipe rings connecting the pipes to the horizontal channels were also tested (referred as “C6”) for both, channel and rod trapeze installations. These components significantly affect the performance of the suspended piping trapezes because



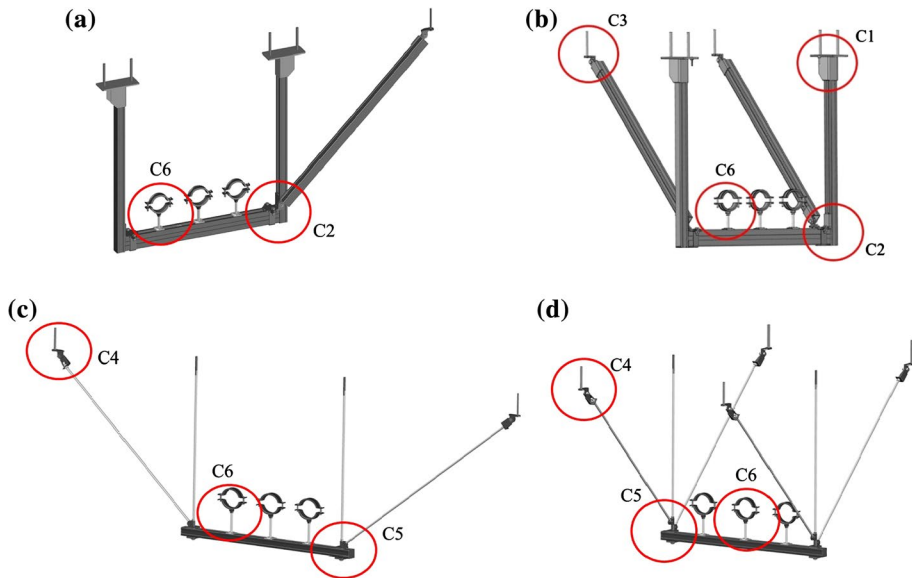


**Fig. 4** Critical components (C1–C6) tested for each suspended trapeze restraint installations: **a** Trapeze with transverse channel bracing system (SS1), **b** Trapeze with longitudinal channel bracing system (SS2), **c** Trapeze with transverse rod bracing system (SS3), **d** Trapeze with longitudinal rod bracing system (SS4)

they transfer directly the seismic load from the pipes to the trapeze installations. Two typologies of pipe rings were tested and were referred as “soft” and “stiff” pipe rings. In a soft pipe ring, a layer of insulation rubber is inserted between the inner surface of the pipe ring and the outer surface of the pipe. In a stiff pipe ring, the pipe is directly in contact with the pipe rings (i.e. steel-to-steel interface). The pipe rings are torqued to the threaded rod with a moment force that is related to the diameter of the threaded rod, which prevent the rotation around the Z axes.

## 4.2 Description of test set-up and loading protocol

A special experimental set-up was designed to conduct the monotonic and reverse cyclic tests on each of the selected components. The experimental set-up needed to be modified quickly to accommodate the geometry of the component to be tested and the loading direction. A universal testing machine was used to perform the monotonic and reverse cyclic tests in displacement control. An array of potentiometers and laser measurement instruments was used to measure displacements at key locations on the test specimens and to record the information required for the numerical modelling.

Table 3 lists all the details of the 44 component tests that were carried out during the experimental program. For each component and loading direction, one monotonic and three cyclic tests were performed. The monotonic tests were also used to calibrate the cyclic loading protocol used in the testing program, as described below. As suggested by FEMA 461 (2007), quasi-static cyclic loading protocol are suitable to obtain data on hysteretic characteristics of the components that can be used to develop analytical and numerical models representative of the subsystems in which the tested components are installed.

Table 2 Description of the tested critical components

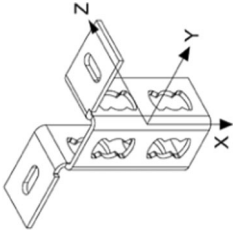
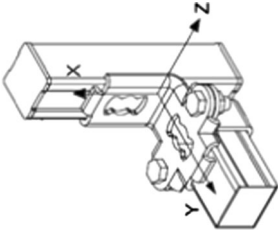
Component ID	Figure	Sub-assembly	Description
C1		SS1 SS2	Rail support connecting the vertical channel to the supporting structure
C2		SS1 SS2	Connection between the vertical and horizontal channels. This component is also used in combination with component C3 to connect the vertical and diagonal channels



Table 2 (continued)

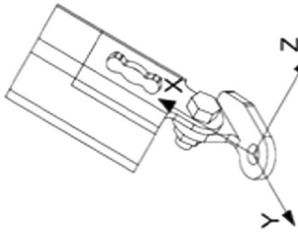
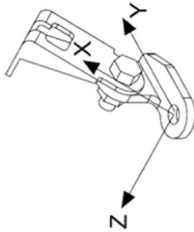
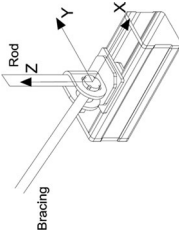
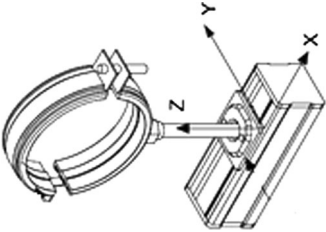
Component ID	Figure	Sub-assembly	Description
C3		SS1 SS2	Hinge connecting the diagonal channels to the supporting structure and component C2
C4		SS3 SS4	Hinge connecting the diagonal rods and the supporting structure
C5		SS3 SS4	Hinge connecting the diagonal and vertical rods

Table 2 (continued)

Component ID	Figure	Sub-assembly	Description
C6		SS1 SS2 SS3 SS4	Connection between the pipes and the horizontal channel. The pipe ring could be installed with (soft pipe ring) or without (stiff pipe ring) insulation

**Table 3** Description of experimental program

Component ID	Loading direction <sup>a</sup>	Loading parameter	Number of mono-tonic tests	Number of cyclic tests
C1	Y	Bending moment	1	3
	Z	Bending moment	1	3
C2	Z	Bending moment	1	3
C3	X	Axial force	1	3
C4	X	Axial force	1	3
C5	X–Z	Axial force	1	3
	Y–Z	Axial force	1	3
C6-Stiff	X	Shear force	1	3
	Y	Shear force	1	3
C6-Soft	X	Shear force	1	3
	Y	Shear force	1	3
Total			11	33

<sup>a</sup>Loading direction for each test is indicated in Figs. 5, 6, 7, 8 and 9

For each component, different loading conditions were applied to investigate the response in the directions of interest in the suspended piping trapeze installations. Figure 5 shows the experimental set-up developed to evaluate the hysteretic behaviour of component C1. The moment capacity in the two main directions (around the Z and Y axes) was evaluated by applying a displacement history to a steel channel connected to the component (Fig. 5a and b). The displacement history was not directly applied to the channel but was transferred through a diffusion steel plate (Fig. 5b). The component was bolted to a rigid steel support fixed to the lower jaw of the testing machine.

The connection between the horizontal and vertical channels (component C2) was tested to assess its moment capacity (around the Z axis). The test set-up designed to evaluate the moment capacity of the component C2 consists of a horizontal channel connected to a vertical channel through component C2. The horizontal channel was bolted to the supporting

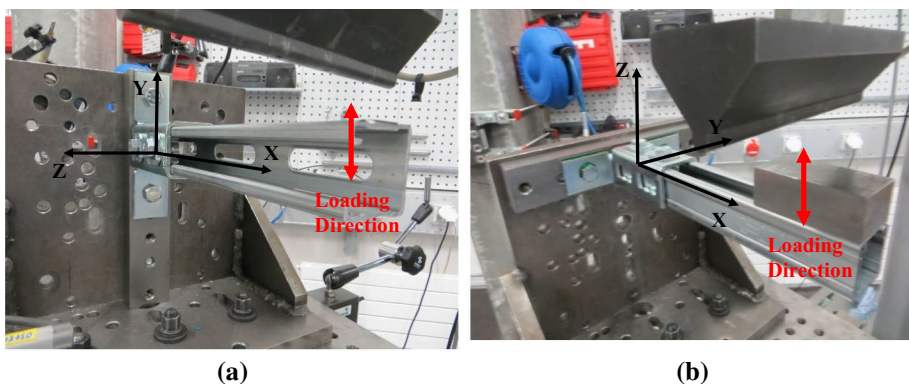


**Fig. 5** Experimental set-up component C1: **a** monotonic and cyclic tests in Y direction, **b** monotonic and cyclic tests in Z direction

**Fig. 6** Experimental set-up for component C2

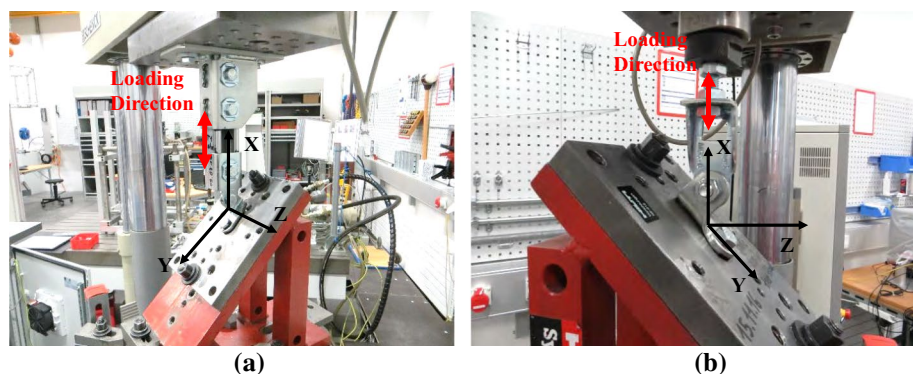


**Fig. 7** Experimental set-up for component C3 and C4: **a** axial capacity for channel configuration, **b** axial capacity for rod configuration

steel plate, while the displacement history was applied to the vertical channel through a diffusion steel plate (Fig. 6).

Component C3 was bolted to a rigid steel supporting frame connected to the lower jaw of the testing machine and inclined at  $45^\circ$  in order to investigate its axial capacity (X direction). The load was applied to the component through a channel element fixed to the upper jaw of the testing machine (Fig. 7a). A similar set-up was used to test component C4, but in this case the load was transferred to the component through a rod element (Fig. 7b).

The axial capacity of component C5 was investigated by two loading conditions. In the first condition, one brace was installed in the transverse (X–Z) direction (Fig. 8a) while in the second condition, the brace was installed in the longitudinal (Y–Z) direction (Fig. 8b). The component was connected to a horizontal channel bolted to a rigid steel support inclined at  $45^\circ$ .

Finally, 16 different tests were performed to investigate the cyclic behaviour of the pipe ring connections. The pipe rings were tested in the transverse (X) and longitudinal (Y) directions (Fig. 9a, b) with and without the introduction of insulation (soft and stiff pipe rings). The displacement history was applied to the pipe ring trough the pipes. For the tests in the transverse direction, the pipe was connected to a rigid steel support, while for the tests in the longitudinal direction the pipe was directly fixed to the upper jaw of the testing machine.

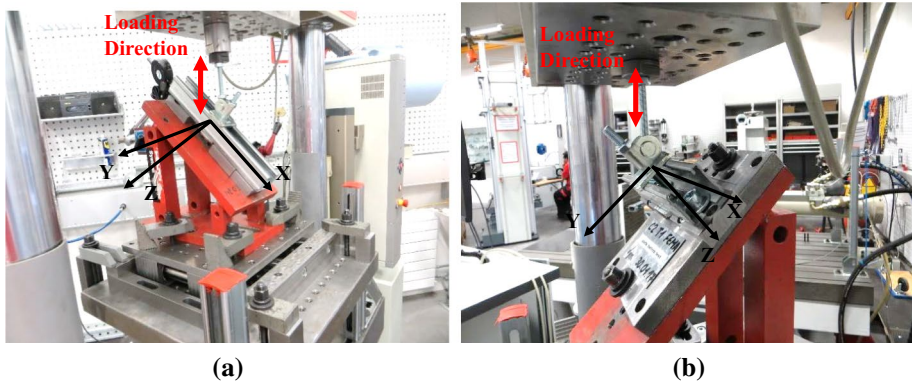


**Fig. 8** Experimental set-up for component C5: **a** axial capacity in the transverse direction, **b** axial capacity in the longitudinal direction

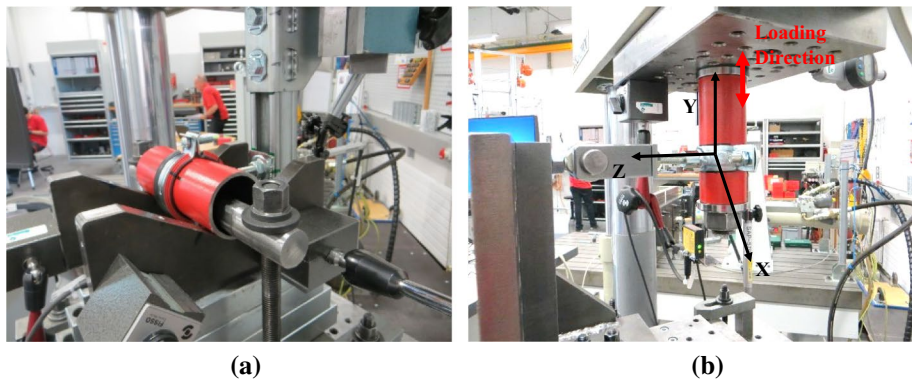


**Fig. 9** Experimental set-up for component C6: **a** shear capacity in the transverse direction, **b** shear capacity in the longitudinal direction

The cyclic tests were carried out following the FEMA 461 quasi-static cyclic loading protocol (FEMA 2007). A recent study concluded that this protocol is the most suitable for the assessment of the hysteretic behaviour of suspended piping restraint components and to observe the inelastic response and damage propagation during the entire deformation range (Filiatrault et al. 2018b). The loading history consists of repeated cycles of step-wise increasing deformation amplitudes. In this study, two cycles at each amplitude were considered. The main parameters necessary to define the FEMA 461 loading protocol are:

- $D_o$ : target smallest deformation amplitude of the loading history;
- $D_m$ : target maximum deformation amplitude of the loading history;
- $n$ : number of steps in the loading history; and
- $a_i$ : amplitude of the cycles.

The amplitude  $a_{i+1}$  of the step  $i + 1$  is given by:

$$\frac{a_{i+1}}{a_n} = 1.4 \frac{a_i}{a_n} \quad (1)$$

where  $a_i$  is the amplitude of the preceding step  $i$  and  $a_n$  is the amplitude of the step close to the target  $D_m$ . If a specimen had not reached the final damage state at  $D_m$ , the amplitude was further increased by constant increment equal to  $0.3 D_m$ . The parameter  $D_m$  is the anticipated deformation at which the most severe damage level (i.e. failure) is expected to occur.

The amplitude increment is controlled by the number of steps. As suggested in FEMA 461, the minimum number of steps were assumed equal to 10, with  $a_1 = 0.048 D_m$  (this value corresponds to  $D_o$ ). The monotonic tests to estimate  $D_m$  were performed in displacement control up to the failure of the components or up to a decrease of 20% of the maximum load achieved during the test. A slow loading rate was selected to avoid inducing inertia effects.

### 4.3 Monotonic and cyclic test results

In this section, the main results of the component experimental program are presented in terms of load–displacement response and observed damage. For each component tested, and for each loading direction, the load–displacement response measured during the monotonic test is compared with those obtained during the cyclic tests.

Figure 10 shows the load–displacement response for component C1. The cyclic tests in the X and Z directions were performed by applying the displacement history only in one direction due to set-up restraints. The load values in the vertical axes in Fig. 10 are provided as percentage of the maximum force ( $F_{max}$ ) obtained in all the tests conducted on component C1. Each specimen was cycled from the zero position to the maximum displacement and then returned to the zero position. The yielding of the components was observed in both monotonic and cyclic tests (Fig. 11a, b). In all the monotonic and cyclic tests, the universal testing machine reached its travel limits before failures of the C1 test specimens could be observed.

Component C2 was tested to evaluate its moment capacity and exhibited a ductile behaviour (Fig. 12). The yielding of the component, associated with a separation of the horizontal and vertical channels, was observed during the tests (Fig. 13).

Components C3 and C4 were tested in the axial direction to evaluate the maximum load at which the diagonal brace disconnected from the component. Figure 14 shows the

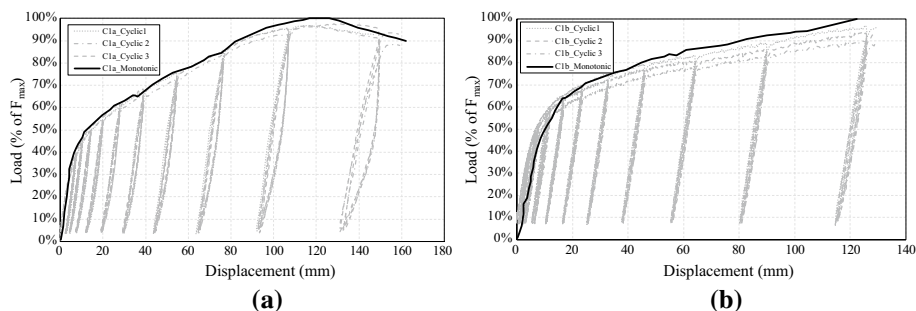


**Fig. 10** Load-displacement response for component C1: **a** Y direction, **b** Z direction



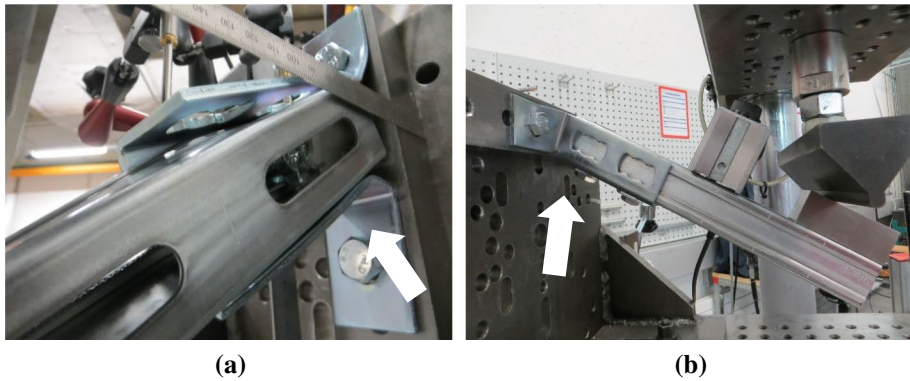


**Fig. 11** Damage observed during tests on component C1: **a** Y direction, **b** Z direction

**Fig. 12** Load-displacement response for component C2

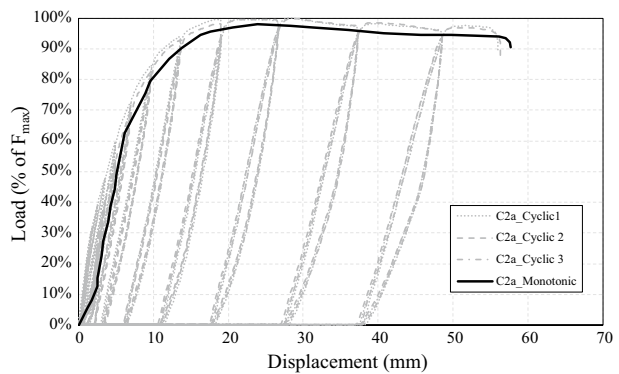
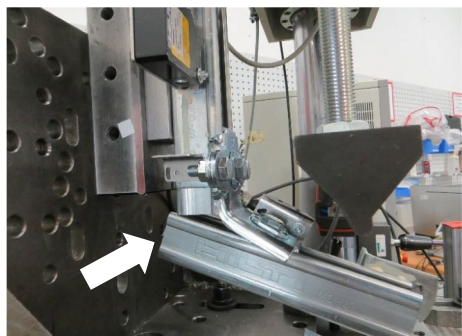


**Fig. 13** Damage observed during tests on component C2



load–displacement response for components C3 and C4. Again, the load values are provided as a percentage of the maximum force ( $F_{\max}$ ) obtained in all the tests conducted on components C3 and C4. The shearing of the thread between the component and the diagonal channel was observed at the end of the tests (Fig. 15a). Component C4 exhibited a high ductility (Fig. 14b). In all tests, the failure of the components was observed



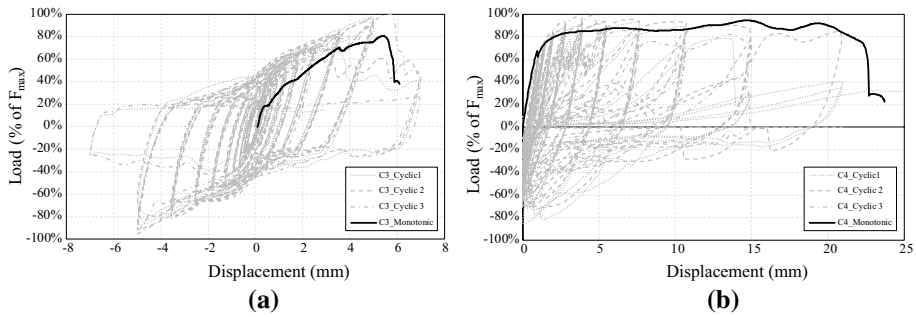


**Fig. 14** Load-displacement response for components C3 and C4: **a** X direction for component C3, **b** X direction for component C4



**Fig. 15** Damage observed during tests on components C3 and C4: **a** X direction for component C3, **b** X direction for component C4

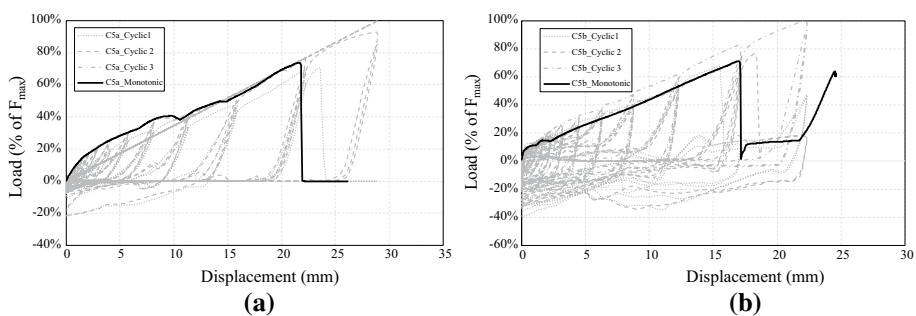


**Fig. 16** Load-displacement response for component C5: **a** X–Z direction (45°), **b** Y–Z direction (45°)

and was due to the high deformations of the connection between the threaded rod and the tested component (Fig. 15b).

Figure 16 shows the load–displacement response of component C5 tested in the transverse (X–Z) and longitudinal (Y–Z) direction. The failure of the component, in both directions, occurred at significantly smaller displacements in the monotonic tests than in the

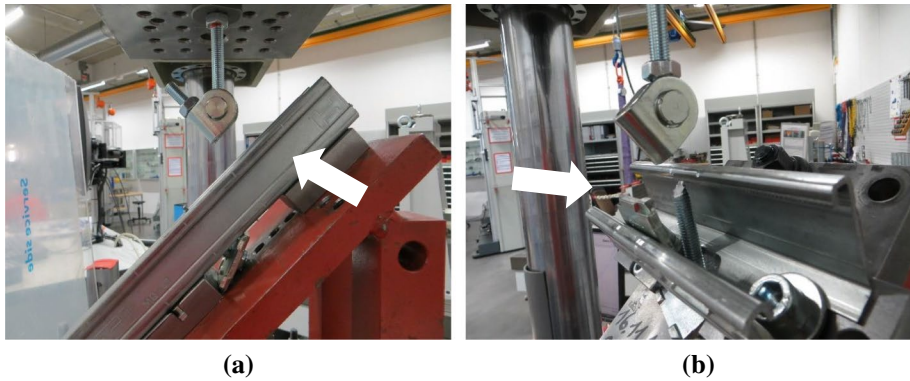


**Fig. 17** Damage observed during tests on component C5: **a** X–Z direction (45°), **b** Y–Z direction (45°)

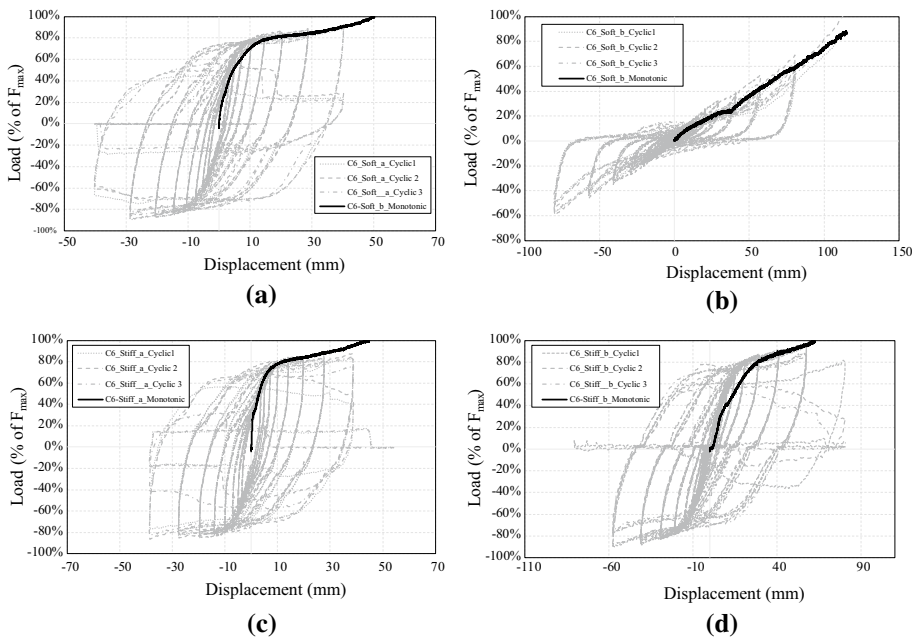


**Fig. 18** Load-displacement response for component C6: **a** X direction for soft pipe rings, **b** Y direction for soft pipe rings, **c** X direction for stiff pipe rings, **d** Y direction for stiff pipe rings

cyclic tests. In the transverse direction, the failure was related to the sliding of the component in the horizontal channel until the end of the hole present in the channel, then the failure of the diagonal threaded rods was observed (Fig. 17a). In the longitudinal direction, the opening of the channel and the failure of the threaded rods were observed (Fig. 17b).

Component C6 was tested in two directions considering two different configurations: with and without insulation. Figure 18a and b show the load–displacement responses of component C6 when the insulation was introduced (soft pipe rings), while Fig. 18c and d show the associated load–displacement response without insulation (stiff pipe rings).

Again, the load values are provided as a percentage of the maximum force ( $F_{\max}$ ) obtained in all the tests conducted on component C6. Similar maximum loads were recorded with or without the insulation. The insulation, on the other hand, had a significant influence on the displacement capacities of the specimens in the longitudinal direction. The maximum displacement recorded in the longitudinal (Y) direction was equal to 100 mm when the insulation was present. The corresponding maximum longitudinal displacement was only 63 mm when the insulation was removed. The deformation of the horizontal channel, as well as the shear failure of the threaded rods, were observed in the transverse (X) direction (Fig. 19a and c). The shear failure of the threaded rods also occurred in the longitudinal (Y) direction for the configuration without insulation (Fig. 19d), while the sliding of the component in the pipe without any failure was observed for the insulated pipe rings (Fig. 19b).

## 5 Component numerical modelling

The development of numerical models to simulate the monotonic response (backbone curve) of the suspended piping trapeze restraint installations described in Sect. 2 is based on modelling assumptions resulting from the component testing described in Sect. 4 and from previous observations of the benchmark sub-assembly tests reported by Perrone et al.

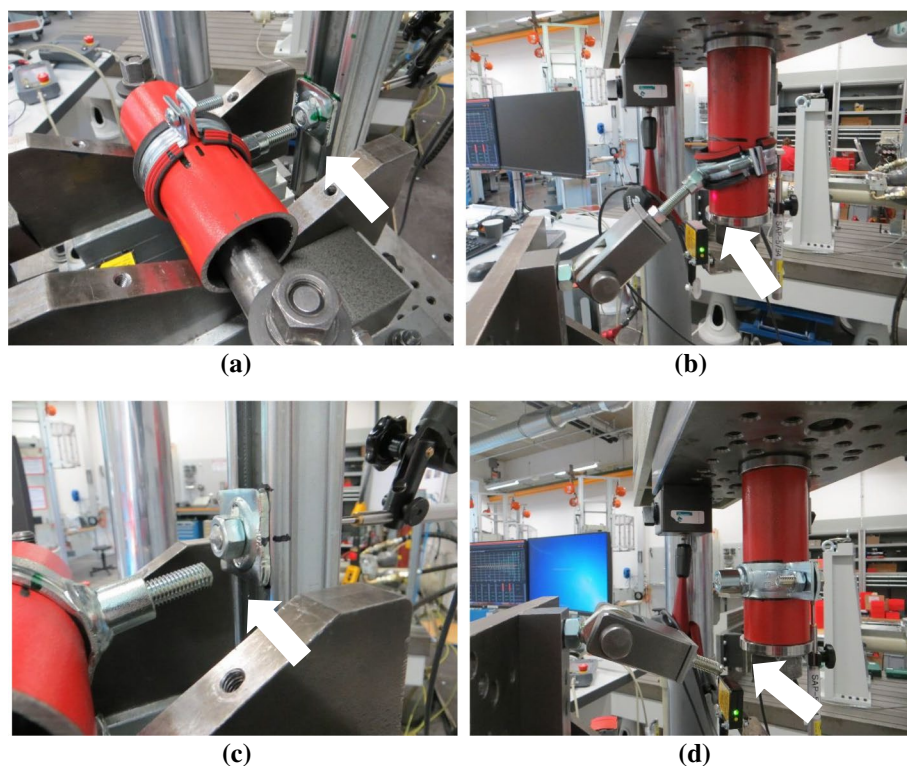


**Fig. 19** Damage observed during tests on component C6: **a** X direction for soft pipe rings, **b** Y direction for soft pipe rings, **c** X direction for stiff pipe rings, **d** Y direction for stiff pipe rings

(2020) and briefly discussed in Sect. 3. Based on the analysis of the benchmark sub-assembly tests, the components were divided in two categories:

1. Components that require detailed numerical modelling. These components significantly affect the global behaviour of the suspended piping trapeze restraint installations. The performance of these components is dependent on the geometry (e.g. distance from pipe to channel) and their interactions with other components. Detailed mechanics-based numerical models were developed based on the component testing and were introduced in the sub-assembly numerical models, as discussed below (see Sect. 6). The numerical modelling of the components (as well as of the sub-assemblies) was undertaken using the open source finite element (FE) software OpenSees (McKenna et al. 2006).
2. Components for which the performance parameters obtained from the component testing (i.e. stiffness and strength) were directly implemented in the sub-assembly numerical models without the development of detailed modelling. For the installations considered herein, these components were not directly involved in the failure modes observed during the benchmark tests. Their mechanical properties are introduced in the sub-assembly numerical models by means of simple link and hinge elements in order to provide the correct stiffness and strength to each element and to allow a generalization of the numerical models for future parametric studies.

### 5.1 Modelling of component C1

Component C1 (rail support connecting the vertical channel to the supporting structure) does not require a specific mechanics-based numerical model to simulate its behaviour in the sub-assembly models. The simplicity of the component, and the perfect correspondence between the configuration in the experimental set-up and in the installation conditions, allows to directly introduce the mechanical properties of the component in the sub-assembly numerical models. In particular, as further discussed in Sect. 6, the stiffness and the strength of the component in the two main bending directions were implemented as restraint boundary conditions of the vertical channels.

### 5.2 Modelling of component C2

A simple mechanics-based model, consisting of an assemblage of elastic, rigid and fibre beam elements, was developed to reproduce the experimental response of component C2 (connection between vertical/diagonal and horizontal channels). Figure 20 illustrates both the numerical model as well as one of the L-shaped specimens before testing. Key elements of the proposed model and the geometry of the corresponding specimen's components are shown in this figure.

As can be seen from Fig. 20a, two force-based fiber nonlinear beam-column elements, each with five integration points, were included in the model to simulate the flexural response of the L-shaped steel plate connection between the horizontal and vertical channels. The  $41 \times 4$  mm plate was modelled as a rectangular cross section discretized in  $82 \times 16$  fibres (plate depth  $\times$  plate thickness) with a uniaxial hysteretic material model. A one-to-two correspondence was assumed between the structural members and model elements for both the horizontal and vertical portions of the L-shaped channel-to-channel connection, meaning that each portion was split into two model elements in correspondence to the position where the channel is fixed to the plate. Rigid elements connect the

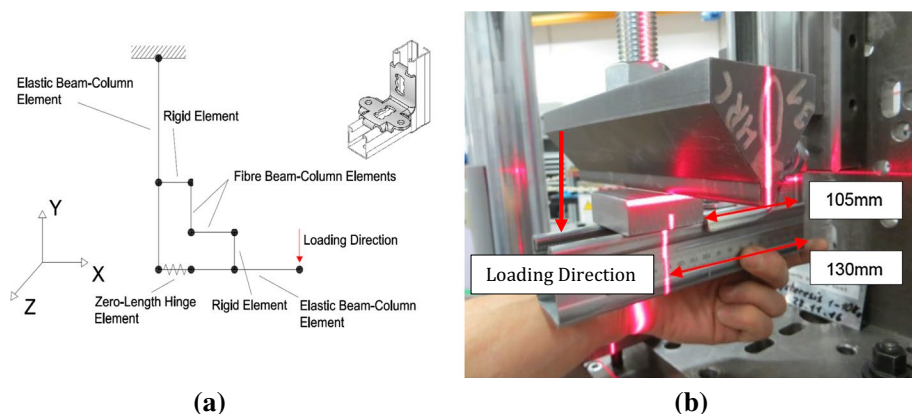


**Fig. 20** Mechanics-based numerical model for component C2: **a** schematic of the adopted numerical representation, **b** geometry of the tested specimen

fibre elements to the channel's horizontal and vertical portions, each of which was discretised into two elastic beam-column elements accordingly. A zero-length hinge element was also included in the model to release the in-plane rotation between the horizontal and vertical portions of the channel.

The monotonic pushdown analysis, whose results are presented in Fig. 21, was performed in displacement-control mode by imposing a 0.1 mm displacement downward for each loading step, taking also into account geometric nonlinearities through the P- $\Delta$  geometric transformation. A good agreement can be observed between the experimental response and the numerical predictions for the entire range of imposed displacements, implying that the model described above (Fig. 20a) satisfactorily reproduced both the initial testing stages (i.e. elastic stiffness of the system/specimen) as well as the moderate/large displacements (i.e. yield and ultimate strength). Even though this mechanics-based model is accurate and computationally efficient, the computational costs could be further reduced for the sub-assembly modelling, by condensing the model into a much simpler rotational spring. The experimental and numerical force–displacement response curves shown in Fig. 21a could be converted into the moment–rotation relationships presented in Fig. 21b, by assuming a 130 mm lever arm (as shown in Fig. 20b). The Pinching4 model

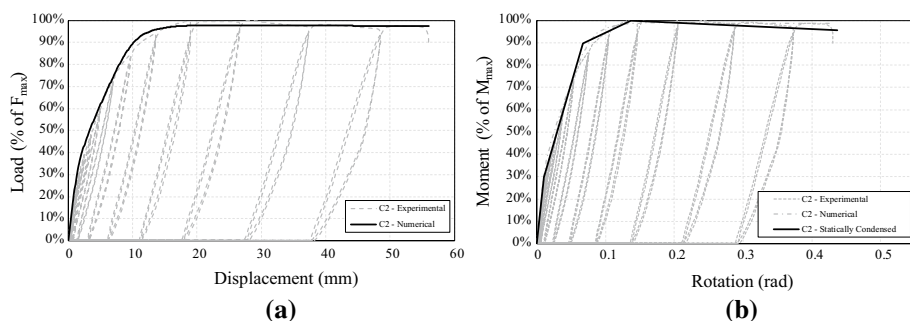


**Fig. 21** Comparison between experimental results and numerical predictions for component C2: **a** mechanics-based model, **b** static condensation using Pinching4 model



available in OpenSees was used to define a simple model to be introduced in the sub-assembly models. This model provides the user/analyst with four adjustable floating points on its response envelope.

### 5.3 Modelling of component C3

Component C3 (hinge connecting the diagonal channels to the supporting structure) does not require the definition of a detailed mechanics-based numerical model because it was not involved in the failure modes of the tested sub-assemblies (Perrone et al. 2020). The maximum strength of component C3 is accounted for in the restraint boundary conditions of the sub-assembly numerical models. Component C3 is also used in combination with component C2 in order to connect the diagonal brace to the horizontal channel in sub-assemblies SS1 and SS2. A detailed discussion on how the connection between components C2 and C3 is modelled is provided in Sect. 6.

### 5.4 Modelling of component C4

Figure 22 illustrates the fibre-based numerical model developed to predict the response of component C4 (hinge connecting the diagonal rods to the supporting structure), along with a photograph of one of the C4 specimens during testing. As shown in Fig. 22a, the proposed numerical model consists of an assembly of seven nonlinear beam-column elements featuring different rectangular and U-shaped cross sections used to reproduce the stress–strain response of each portion of the component. The force-based fibre elements were assembled to simulate the geometry and geometric eccentricities of the specimen, thus reproducing its behaviour, with the latter being driven by a combination of axial and flexural responses.

The rectangular base section was a  $24 \times 6$  mm plate and was modelled as a rectangular cross section discretised in 48 and 12 fibres along the plate depth and thickness, respectively. The element at its top was also modelled as a rectangular plate with depth

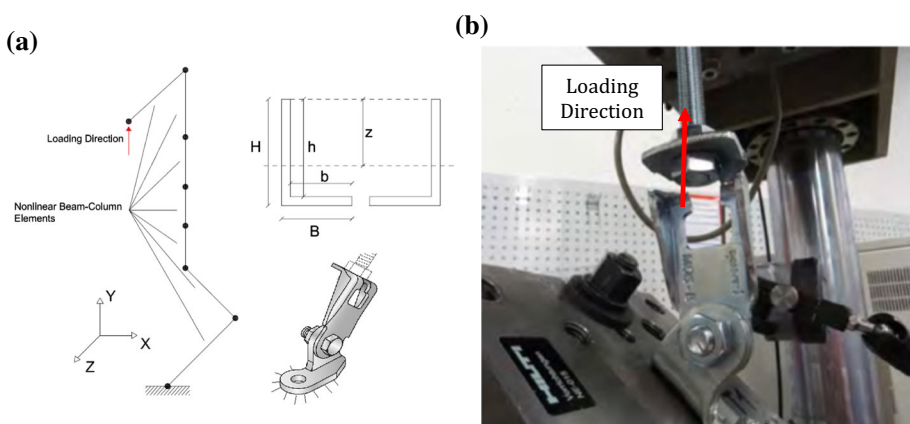


**Fig. 22** Fibre-based numerical model for component C4: **a** schematic of the adopted numerical representation, **b** geometry of the tested specimen

and thickness equal to 28 and 6 mm, respectively. The fibre size was kept constant for the other nonlinear beam-column elements, one of which features a rectangular cross section and the other three have U-shaped cross sections with and without holes. The seventh fibre-based element of the assembly, whose longitudinal axis is oriented along the Z axis (see Fig. 22a), was again modelled as a rectangular cross section with  $34 \times 4$  mm dimensions and  $68 \times 8$  fibres. Each fibre element was characterized by five integration points and the potential geometric nonlinearities were taken into account by the P- $\Delta$  geometric transformation.

The comparison between the experimental and numerical force–displacement response curves of component C4 is presented in Fig. 23a. Similar results could be also obtained by a condensed approach using the Pinching4 model available in OpenSees (Fig. 23b),

## 5.5 Modelling of component C5

The results of the benchmark tests clearly showed that the buckling of the diagonal and vertical rods governed the response of the rod configurations (SS3 and SS4), before the failure of the connections between the diagonal and vertical rods. For this reason, only the maximum capacity of component C5 (hinge connecting diagonal and vertical rods) was directly introduced in the sub-assembly numerical models, as further discussed in Sect. 6.

## 5.6 Modelling of component C6

Figure 24 illustrates the numerical models of component C6 (connection between the pipes and horizontal channel) in the longitudinal direction and shows its component testing set-up that identifies the geometry and configuration of the model elements.

As shown in Fig. 24a, the proposed numerical model consists of an assembly of one force-based fibre element for the threaded rod connecting the channel to the pipe ring, one elastic beam-column element simulating the channel and a series of rigid elements, the latter being modelled as elastic beam-column elements with high stiffness properties. The rigid elements are in series: the distance between the barycentre of the pipe and the pipe ring, R3, which is the distance between the pipe and the fibre element, R5 that consists in the distance between the threaded rod and the channel. The elements R3 and R5 are considered rigid due to the higher thickness of their cross section with respect to the stiffness of the threaded rod. Figure 24b shows the way these rigid elements are assembled together and indicates where

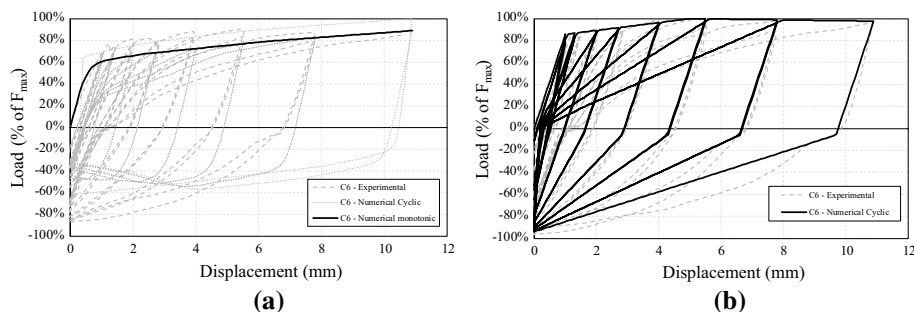


**Fig. 23** Comparison between experimental results and numerical predictions for component C4: **a** fibre-based model, **b** static condensation using Pinching4 model



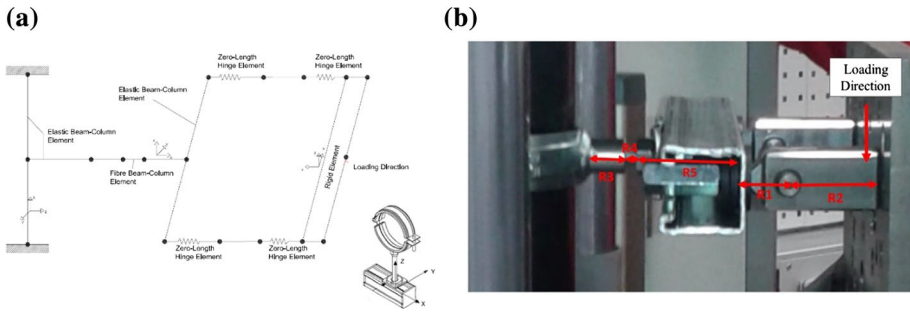


**Fig. 24** Mechanics-based numerical model for component C6: **a** schematic of the adopted numerical representation, **b** geometry of the testing set-up and rigid links

flexural releases have been included (R1 represents the distance between the hinge and the horizontal channel, R2 is the distance between the fix point and the hinge and R4 is the length of the fibre element). Four zero-length elements with very low flexural stiffness were introduced in the numerical model in order to release rotations and to simulate the cylindrical hinges of the testing set-up. The force-based nonlinear beam-column element was assumed to have five integration points, whereas the circular fibre section was discretised into  $8 \times 8$  subdivisions along the radius and circumference using the circular patch command available in the OpenSees software. Maximum iterations and convergence tolerance (at the element level) were set to 10 and  $10^{-16}$ , respectively. The uniaxial hysteretic material model was used to simulate the stress–strain response of steel fibres, accounting for permanent inelastic deformations exhibited by them. The material model parameters used for simulation are reported in Table 4.

In Table 4,  $s_{jp}$  and  $e_{jp}$  are the stress and strain at the  $j$ th point of the envelope in the positive direction. The material model was set to be symmetrical, meaning that  $s_{jn} = s_{jp}$  and  $e_{jn} = e_{jp}$ , where the sub-script  $n$  identifies the counterpart stress and strain on the negative side of the backbone curve. The pinching factors (for stress and strain during reloading) were set to 0.5 and 0.2, although the component and sub-assembly models presented in this study are mainly concerned with monotonic simulations.

For modelling the channel, the Bernoulli beam element implemented in OpenSees relies upon a six degrees-of-freedom (DOFs) beam formulation, which in turn implies that the torsional stiffness value,  $K_7$ , used as input should be adapted according to Eq. (2):

$$K_7 = \frac{6}{5} \frac{GI_t}{L} + \frac{12EI_w}{L^3} \quad (2)$$

where  $GI_t/L$  is the term associated with uniform torsion,  $G$  is the tangential modulus,  $E$  is the Young's modulus,  $L$  is the length and  $I$  is the second moment of area, whilst the sub-scripts  $t$  and  $w$  stand for uniform torsion and warping, respectively. The stiffness  $K_7$  accounts for the contribution that is expected by a more sophisticated seven DOFs beam formulation, in a computationally efficient manner.

**Table 4** Parameters for uniaxial hysteretic material model

$s_{1p}$ (MPa)	$e_{1p}$ (–)	$s_{2p}$ (MPa)	$e_{2p}$ (–)	$s_{3p}$ (MPa)	$e_{3p}$ (–)
340	$1.7 \times 10^{-3}$	810	$4.1 \times 10^{-2}$	1600	3.0

Figure 25 compares the experimental results obtained from the component testing of a rigid pipe ring (i.e. component C6) with the cyclic and monotonic numerical predictions. The relatively simple model described above reproduces reasonably accurately the response of the tested specimen for the entire range of imposed displacements.

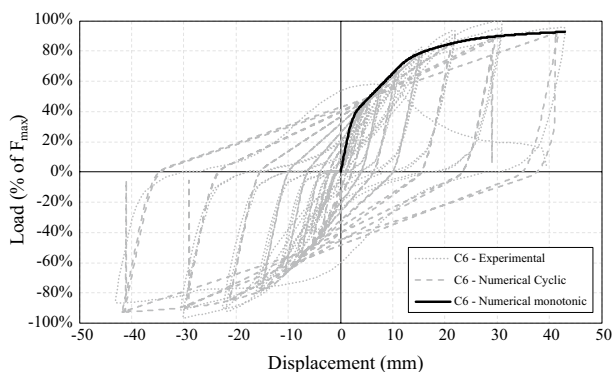
Focusing on key aspects for sub-assembly modelling, the above curves (Fig. 25) lay evident that both the elastic stiffness of the specimen as well as its peak and ultimate strength can be predicted in a satisfactorily manner with a mismatch between experimental and numerical data up to approximately 6%. For the peak strength, the percentage difference is 6% at a displacement of 31 mm (and 18% strain) and, for the ultimate resistance, the percentage difference is 3% at a displacement of 43 mm (and 28% strain). The prediction capability of the numerical model proved the effectiveness of the modelling assumptions used to model the channel and the pipe ring, this is of paramount importance considering that both components played an important role in the response of the tested sub-assemblies.

A numerical model to simulate the pipe rings behaviour in the transversal direction was not developed because, based on the benchmark sub-assembly tests, this component did not affect the monotonic and cyclic response of the sub-assemblies. Therefore, the numerical models described in Sect. 6 only include the measured maximum strength of the pipe rings in the transverse direction.

The pipe rings with insulation (soft pipe rings) were not taken into account at this stage of the study because the benchmark sub-assembly tests did not include any insulation. Two different approaches could be used to account of the soft pipe rings. In the first approach, the insulation could be introduced in the mechanics-based numerical model of component C6 by means of shear springs calibrated according to the test results. Even if from a theoretical point of view this approach could be efficient, some numerical issues could make very difficult its application into practice. For this reason, it is suggested to account for the effect of the insulation on the response of the soft pipe rings by post-processing. Based on the component testing, the ratio between the stiffness of the soft and stiff pipe rings could be evaluated and an amplification factor could be directly applied to the relative displacement of the rigid pipe rings in order to account of the higher displacement in the longitudinal direction due to the rubber deformation. In the transverse direction no modification is required.

The component rupture-driven failure mechanism(s) of the tested sub-assembly specimens (Perrone et al. 2020) makes the relatively straightforward numerical models

**Fig. 25** Comparison between experimental results and numerical predictions for component C6



presented in this section into pivotal building blocks for sub-assembly modelling and analysis, as discussed in the next section.

## 6 Sub-assembly modelling

In this section, the 3D numerical models developed to predict the monotonic response of the suspended piping trapeze restraint installations described in Sect. 2 (SS1–SS4) are presented. The numerical model for each of the four trapeze restraint installations considered predicts the response of a single trapeze with its bracings. The predictions of each numerical model is compared against the average monotonic response of the two corresponding suspended trapeze installations tested simultaneously in the sub-assembly benchmark test described in Sect. 3. Because the numerical models are developed to predict the monotonic response of the analysed suspended piping trapeze restraint installations, considerations on the hysteretic damping are not provided in this work. However, useful details on this issue are provided in Perrone et al. (2020).

All four sub-assembly models include both material nonlinearities (at the element and/or component level) and geometric nonlinearities (using the P- $\Delta$  or co-rotational geometric transformation). Each model includes a different level of sophistication and features according to the expected/observed response from the sub-assembly benchmark testing (Perrone et al. 2020). For the rod configurations (i.e. sub-assemblies SS3 and SS4), the co-rotational transformation was assigned to the diagonal and vertical slender rods, which were found to be prone to buckling, whereas the P- $\Delta$  transformation was considered for both the pipe rings and the horizontal channel, none of which experienced large displacements/rotations during testing. On the other hand, for configurations SS1 and SS2, both of which include channels as bracing system, the P- $\Delta$  geometric transformation was used for all model elements. Moreover, for sub-assemblies SS3 and SS4, diagonal and vertical elements (i.e. rods) were modelled using inelastic force-based fibre elements, whereas elastic beam-column elements were used to simulate the response of diagonal and vertical members of the channel configurations SS1 and SS2.

Finally, for the pipe rings (i.e. component C6), the relatively simple mechanics-based fibre model concept presented in Sect. 5.6 was implemented in the longitudinally loaded sub-assembly models (i.e. configurations SS2 and SS4), whilst fibre elements were replaced by elastic beam-column elements for the transversally loaded sub-assemblies (i.e. configurations SS1 and SS3), given that these latter suspended piping trapeze installations did not exhibit any sort of damage in the pipe rings during the monotonic and cyclic tests, in both channel or rod configurations (Perrone et al. 2020). The possible rotation of the pipes due to impact forces is not considered in this study and should be accounted for in the numerical modelling at the system level.

The general considerations offered above were merged with more specific details collected in Sects. 6.1–6.4, where the key assumptions underlying every sub-assembly model are outlined and discussed case-by-case. Finally, a number of performance parameters necessary for the elaboration of performance-based seismic design procedures for suspended piping restraint installations were extracted from the experimental pushover curves and compared to the predicted values by the numerical models for the four sub-assembly configurations considered.

## 6.1 Modelling of sub-assembly SS1

Figure 26 shows the numerical model developed to predict the monotonic response (backbone curve) of sub-assembly SS1 (trapeze with transverse channel bracing system). The major components of the proposed model include elastic beam-column elements, zero-length hinges, rigid elements and inelastic rotational and axial links assembled together.

For the sub-assembly configuration SS1, the pipe rings did not exhibit damage of any sort and, hence, were modelled using elastic beam-column elements with elastic properties calibrated according to the geometric properties of their cross section and according to the strength obtained from the component test results. Vertical and horizontal rigid elements were used to connect the four pipe rings together and simulate the test setup. Additionally, the equal DOF option available in OpenSees was used in order to constrain the top and bottom nodes of the vertical rigid elements, imposing the four pipes/pipe rings to deform together. Vertical rigid elements were also used to connect the bottom nodes of the four elastic beam-column elements with the horizontal channel underneath the pipe rings. The horizontal channel was modelled by five elastic beam-column elements, with their torsional stiffness calculated in accordance with Eq. (2). Based on the results of the benchmark sub-assembly tests, the torsional stiffness of the horizontal channel did not play any significant role in the response of this sub-assembly system.

Zero-length link elements were included to connect the horizontal and vertical channels, thus modelling the inelastic response of the L-shaped plate for channel-to-channel connection. These zero-length elements considered only the in-plane rotation, whereas the other two rotations and the three translations were simply restrained associating a rigid material model with these DOFs. By contrast, the Pinching4 material model was adopted to simulate the behaviour of the L-shaped plate connection (i.e. component C2).

An inelastic axial link (i.e. zero-length element) was included in the model to simulate the flexural failure mechanism of the brace-to-channel bolted steel plate connection, introducing a limit in the axial resistance of the diagonal brace of the sub-assembly. The resistance of the steel plate (and, hence, of the axial link),  $F$ , was calculated by:

$$F = \frac{M}{e} = \frac{Wf_y}{e} = \frac{2If_y}{me} = \frac{2nm^3f_y}{12me} = \frac{nm^2f_y}{6e} = \frac{6 * 28^2 * 355}{6 * 40} = 7.0 \text{ kN} \quad (3)$$

where  $W$  is plastic modulus of the steel section,  $f_y$  is the yield stress,  $I$  is the second moment of area,  $n$  and  $m$  are the base and height of the plate, and  $e$  is the eccentricity of the brace with respect to the channel. A 30% strength drop was also implemented in the constitutive model of the link after the above capacity was exceeded.

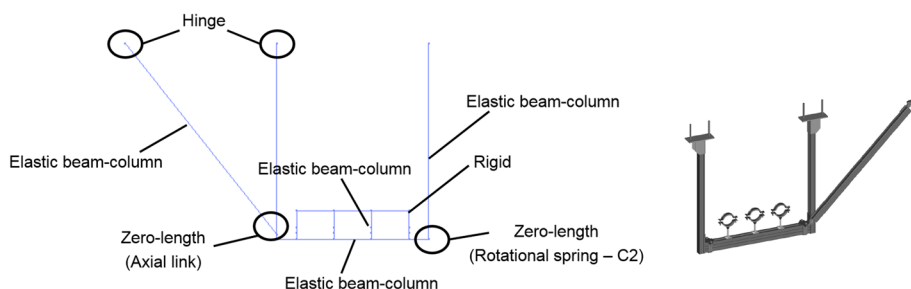


Fig. 26 Numerical model for sub-assembly SS1

Finally, because the diagonal brace member was not subjected to buckling during the benchmark sub-assembly tests, it was modelled as an elastic beam-column element with the geometric properties of the channel's cross section. The connections at the top of the brace and vertical channels were treated/modelled as zero-length spherical hinge elements.

## 6.2 Modelling of sub-assembly SS2

Isometric (3D) and planar views (i.e. top, front and side views) of the numerical model for sub-assembly SS2 (trapeze with longitudinal channel bracing system) are shown in Fig. 27. The element type employed for each member and/or component of sub-assembly SS2 is indicated in the figure.

As shown in Fig. 27, the numerical model developed for sub-assembly SS2 relies upon the mechanics-based model of component C6 (see Sect. 5) for which the pipe rings were modelled using a distributed plasticity approach. Four nonlinear fibre beam-column elements were used to simulate the inelastic response of the four pipe rings, thereby implying that a one-to-one correspondence was assumed between these structural members and the counterpart model elements. Such an assumption is valid as long as the exact force-based formulation is considered, given that the latter does not require any element discretisation. Each force-based fibre element had five integration points, and the circular cross section was discretised by  $8 \times 8$  fibres along the radius and circumference. Similarly, the uniaxial hysteretic material model, with parameters calibrated as reported in Table 4, was employed for the integration of the stress–strain response of each fibre composing the pipe ring's cross section. As implemented in the SS1 sub-assembly model, four vertical rigid elements and three horizontal rigid elements were incorporated in such way that the four pipe rings could be connected together, replicating the loading condition of the experimental setup. The pipelines were prevented from rotating out-of-plane, namely around the longitudinal axis of the horizontal channel.

Four additional rigid elements were included in the SS2 numerical model to connect the bottom nodes of the fibre-based pipe ring elements to the horizontal channel. This horizontal channel was modelled by means of five elastic beam-column elements. Their material properties were calculated according to the elastic properties of the channel's cross section, adjusting also the torsional stiffness in accordance with Eq. (2). This permitted to account

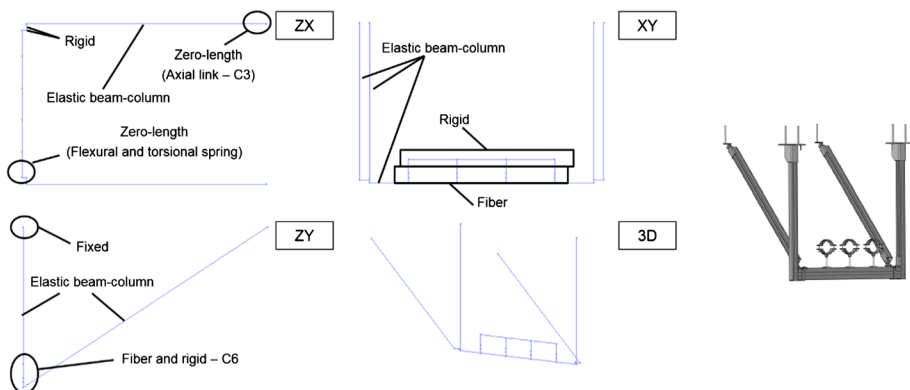


Fig. 27 Numerical model for sub-assembly SS2

for the 7th DOF, within a six-DOF Bernoulli beam formulation, as demonstrated in Sect. 5 for the component modelling of pipe rings.

Furthermore, two zero-length elements, one per each end of the horizontal channel, were included in the model in order to connect the horizontal and vertical channels.

Each of these channels was modelled as a single elastic beam-column element fully fixed (at its top) to the support frame used for testing. The elastic uniaxial material model associated with all six DOFs was used for the definition of the two zero-length elements. The constitutive laws were calibrated in order to reproduce the flexural stiffness of the horizontal channel and the torsional stiffness of the steel plate connecting the horizontal and vertical channels. Uniform torsion was considered and the second moment of area ( $I_t$ ) of each channel was computed according to:

$$I_t = \frac{1}{3}nt^3 = \frac{1}{3} * 41 * 4^3 = 875 \text{ mm}^4 \quad (4)$$

where  $n$  and  $t$  are the base and thickness of the plate. The other degrees of freedom were restrained by assigning high stiffness properties to the elastic material model.

Two orthogonally oriented rigid elements at each channel's end were included to connect the horizontal channel with the diagonal braces, simulating also the effect of geometric eccentricities between the horizontal/vertical channels and the bracing elements of the system. Because buckling was not observed during the benchmark sub-assembly tests, the latter elements were modelled as elastic beam-column elements (without element discretisation) and their elastic properties were again calculated according to the channel's cross section. Their top connections (to the support frame) were also modelled by adding another zero-length axial element per diagonal brace. The stiffness in compression of these elastic axial links was assumed to be equal to the stiffness in tension obtained from component testing. The DOF corresponding to the other two translations were restrained, whereas the three rotations were released.

The monotonic pushover simulation was performed with the braces in compression, which is in agreement with the test procedure that mobilizes the most critical mechanism for the sub-assembly (Perrone et al. 2020). Geometric nonlinearities were taken into account by using the P- $\Delta$  geometric transformation.

### 6.3 Modelling of sub-assembly SS3

A front view of the numerical model developed to simulate the response of sub-assembly SS3 (trapeze with transverse rod bracing system) is shown in Fig. 28. In this case, the diagonal and vertical elements of the suspended piping trapeze installation, which consists of slender rods prone to fail by buckling, were modelled as inelastic force-based fibre beam-column elements. Each nonlinear beam-column element was divided into two sub-elements, each of which had five integration points. The number of sub-elements was selected in order to accurately reproduce the deformed shape obtained in the tests, thereby minimizing the computational efforts. An initial camber, equal to 0.5% of the element's length, was assigned (at mid length) to the two diagonal and the two vertical elements of the sub-assembly so as to make them buckle. The initial imperfection/camber was implemented using the simplest piecewise linear form.

To account for large displacements/rotations that are expected to occur in these elements because of buckling, a co-rotational geometric transformation was used, which applies well to this type of large displacement-small strain problems/kinematics. Within

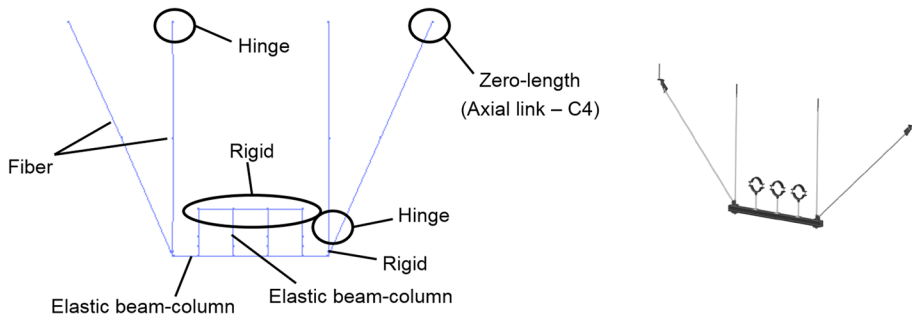


**Fig. 28** Numerical model for sub-assembly SS3

this computational framework, material nonlinearities were also modelled, using a distributed plasticity approach, which relies on the Giuffrè-Menegotto-Pinto constitutive rule (Filippou et al. 1983). To accurately simulate the spreading of inelasticity over the circular cross section of both vertical and diagonal rods, they both were discretised into  $16 \times 6$  subdivisions along the radius and circumference, respectively.

Consistently with the approach adopted for the other transversally loaded sub-assembly (i.e. sub-assembly SS1), the four pipe rings were modelled as four elastic beam-column elements connected together and to the horizontal channel of the suspended piping trapeze installation by means of vertical and horizontal rigid elements. The top and bottom nodes of the vertical rigid elements above the elastic beam-column ones were again constrained to have the same zero-rotation, thus using the equal DOF option in OpenSees to prevent rotations from occurring in this portion of the SS3 sub-assembly. Furthermore, the horizontal channel was connected to the vertical and diagonal rods by means of elastic zero-length elements that simulated a spherical hinge (i.e. a release of bending moment). The top connection of the two vertical rods (with the support frame) was treated and modelled in the same way, whereas that of the diagonal rods was modelled using the Pinching4 material model for component C4 (see Fig. 23b).

## 6.4 Modelling of sub-assembly SS4

Figure 29 shows isometric (3D) and planar views (i.e. top, front and side views) of the numerical model developed for sub-assembly SS4 (trapeze with longitudinal rod bracing system). Since this sub-assembly is also a rod configuration, its response and damage/failure mode were again governed by the buckling of vertical and diagonal elements (Perrone et al. 2020).

The numerical modelling of the SS4 sub-assembly was very similar as that of the SS3 assembly and involved again an initial camber/imperfection and a co-rotational geometric transformation. As shown in Fig. 29, four inelastic force-based fibre elements with five Gauss–Lobatto integration points were used to model the vertical and diagonal rods supporting the horizontal channel. The horizontal channel was in turn modelled as a series of five elastic beam-column elements. Rigid elements were incorporated to connect the channel with the four pipe rings as well as the pipe rings together, as per the test setup (Perrone et al. 2020). Even though the SS4 sub-assembly is a longitudinally loaded trapeze restraint installation, the pipe rings were modelled as elastic beam-column elements, given that no tested specimens exhibited damage in these components (Perrone et al. 2020).



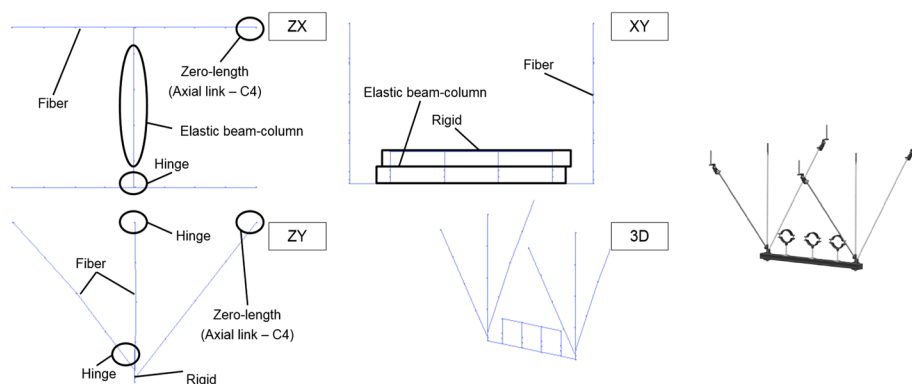


**Fig. 29** Numerical model for sub-assembly SS4

The channel-to-rod connections were assumed to be unable to transfer bending moments between these trapeze elements, and the same assumption was made for the rod-to-support frame connections. Each diagonal rod was assigned the Pinching4 material model developed for component C4.

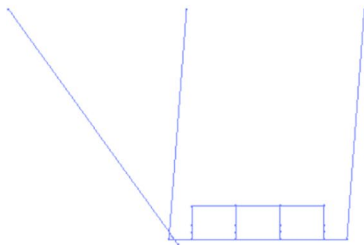
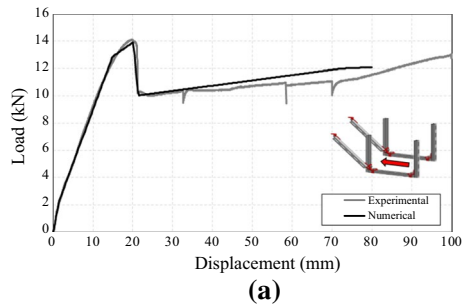
## 6.5 Comparisons between experimental and numerically-predicted sub-assembly monotonic force–displacement curves

To evaluate the accuracy/effectiveness of the modelling approaches discussed in the previous sections, comparisons between numerical predictions and experimental data are systematically presented hereafter, in terms of both monotonic and/or backbone force–displacement response curves as well as damage mechanisms exhibited by the tested sub-assembly specimens. Figure 30 compares the numerical response and deformed shape obtained from monotonic simulation of sub-assembly SS1 with the experimental results.

The numerical model predicts very well the experimental monotonic pushover curve including the sudden strength drop due to the flexural failure mechanism of the brace-to-channel bolted steel plate connection observed during the test. Both elastic stiffness and peak strength were reproduced in the model by the flexural and axial link elements included in the model at the connection level, yielding a discrepancy between numerical and experimental results of only 1–2%. The model is able to predict accurately the experimental response for displacements up to approximately 40 mm. Beyond that point, the model is unable to reproduce the load pick-up exhibited by the specimen during the large-deformation testing stages.

The comparison between the experimental and numerical monotonic response curves obtained for sub-assembly SS2 is presented in Fig. 31a, whereas Fig. 31b shows isometric and side views of the deformed shapes of the model at the ultimate displacement imposed and compares them with a photograph of one of the tested specimens.

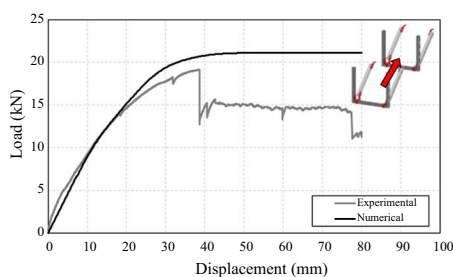
Although larger differences (10–12%) in initial stiffness and peak strength can be observed between the experimental data and numerical predictions, the numerical model can reproduce satisfactorily the damage/failure mode of sub-assembly SS2. For this sub-assembly, the inelastic response of the pipe rings drives the global behaviour of the specimen. The numerical model can reproduce fairly accurately the behaviour of the tested specimen for displacements up to approximately 40 mm, beyond which the experimental

**(b)**

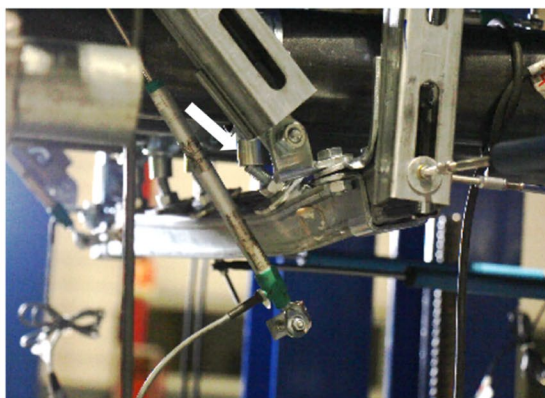
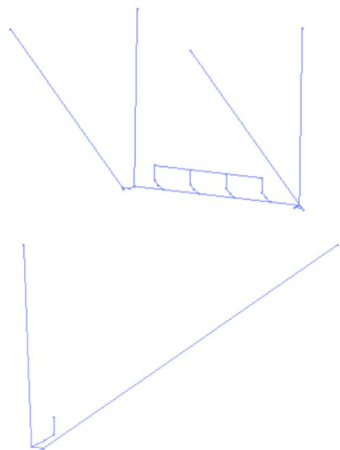
**Fig. 30** Comparison between experimental results and numerical predictions for sub-assembly SS1: **a** monotonic force–displacement response, **b** deformed shape and damage/failure mechanism

force–displacement response curve shows a roughly 35% drop in strength, owing to the rupture of one of the four pipe ring installed on the test specimen. The drop in strength was not accurately predicted by the numerical model because the threaded rods are simulated using fibre beam–column elements that are only able to predict the threshold in terms of strength due to their mathematical formulation. By contrast, after yielding at approximately 20 mm, the numerical response enters in the nonlinear regime, with small level of hardening for displacements in the 20–40 mm range, followed by a flat portion, due to P- $\Delta$  effects. The slope of the numerical response curve matches well that of the experimental curve beyond a displacement of 40 mm.

The comparison between numerically-predicted and experimental monotonic force–displacement responses, shown in Fig. 32, demonstrates the effectiveness of the numerical model in predicting the buckling-driven response of sub-assembly SS3. The initial elastic stiffness of the subassembly is almost perfectly predicted by the numerical model, as shown in Fig. 32a. The peak strength predicted by the numerical model is within 1% as that observed in the test. The largest differences between the predictions of the numerical model and the test results occur in the post-buckling regime, soon after the buckling peak strength is reached for a displacement of approximately 10 mm. Following the buckling of the diagonal rods, the model underestimates by approximately 20% the strength of the test specimen. Even though the model results in a more pronounced post-buckling mode and, hence, a weaker post-buckling strength, the numerical response becomes more stable and aligns much better with the experimental response for displacements ranging between 30



(a)



(b)

**Fig. 31** Comparison between experimental results and numerical predictions for sub-assembly SS2: **a** force–displacement response, **b** deformed shape and damage/failure mechanism

and 75 mm. Figure 32b presents a comparison between the deformed shape of the model at the ultimate displacement imposed and a photograph of one of the specimens during the last testing stage. The numerical model is able to predict the buckling-dominated failure mode of the test specimen.

Figure 33 shows the comparison between the numerical and experimental monotonic pushover curves for sub-assembly SS4. Figure 33a presents both experimental and numerical response curves as well as the relationship between the compression forces recorded in each diagonal rod during the analysis and the lateral displacement applied to the sub-assembly. The right-hand side plot of Fig. 33a, along with the overall force–displacement capacity curve, confirms that the buckling of the slender vertical and diagonal rods supporting the horizontal channel and the pipes is the dominating response mechanism of the analysed/tested sub-assembly. Additionally, the isometric and side views of the deformed shapes at maximum displacement predicted by the numerical model is compared against a photograph of the specimen at failure. Again, the numerical model is able to capture well the damage/failure mode of the test specimen.

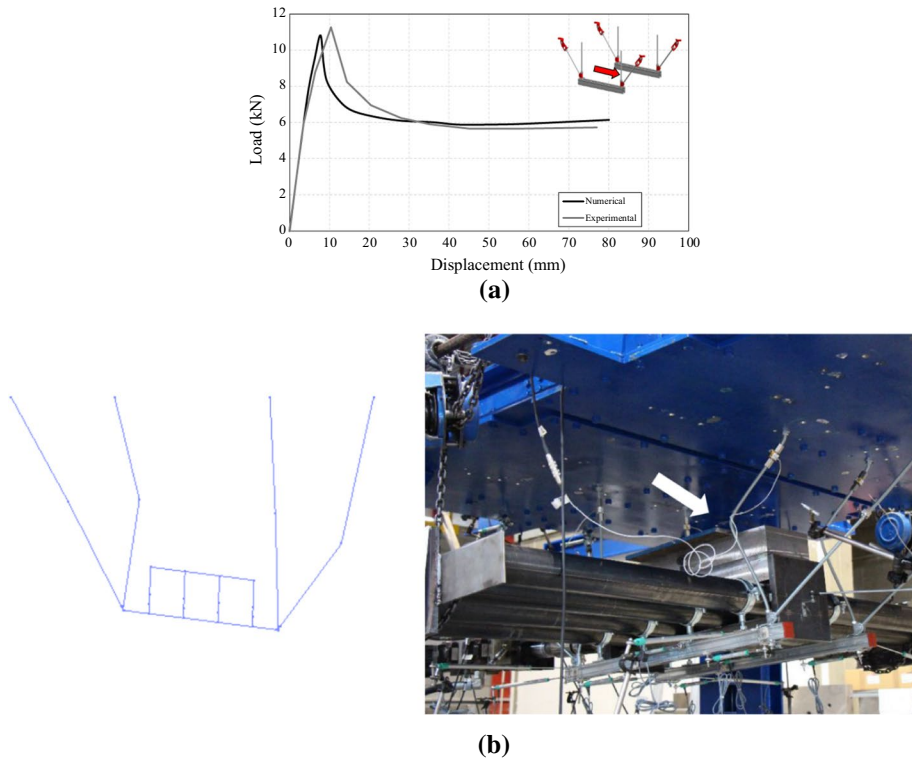


**Fig. 32** Comparison between experimental results and numerical predictions for sub-assembly SS3: **a** force–displacement response, **b** deformed shape and damage/failure mechanism

## 6.6 Comparisons between experimental and numerically-predicted performance parameters

The performance-based seismic design of suspended piping restraint installations requires the definition of performance parameters that characterize their monotonic and cyclic responses and that can be linked to performance objectives. Based on the FEMA P-795 (FEMA 2011) methodology for structural elements, some simple performance parameters can be defined based on the results of the monotonic and cyclic tests conducted on the suspended piping restraints or based on numerical models such as those developed in the previous section. These performance parameters can then be correlated to various damage states observed during the tests or following real earthquake shaking. The following three performance parameters were identified as the most critical for the elaboration of performance-based seismic design procedures for suspended piping restraint installations (Perrone et al. 2020):

1. The maximum load capacity ( $Q_M$ );
2. The  $I$ =initial stiffness ( $K_I$ ) based on force and deformation at  $0.4 Q_M$ ;

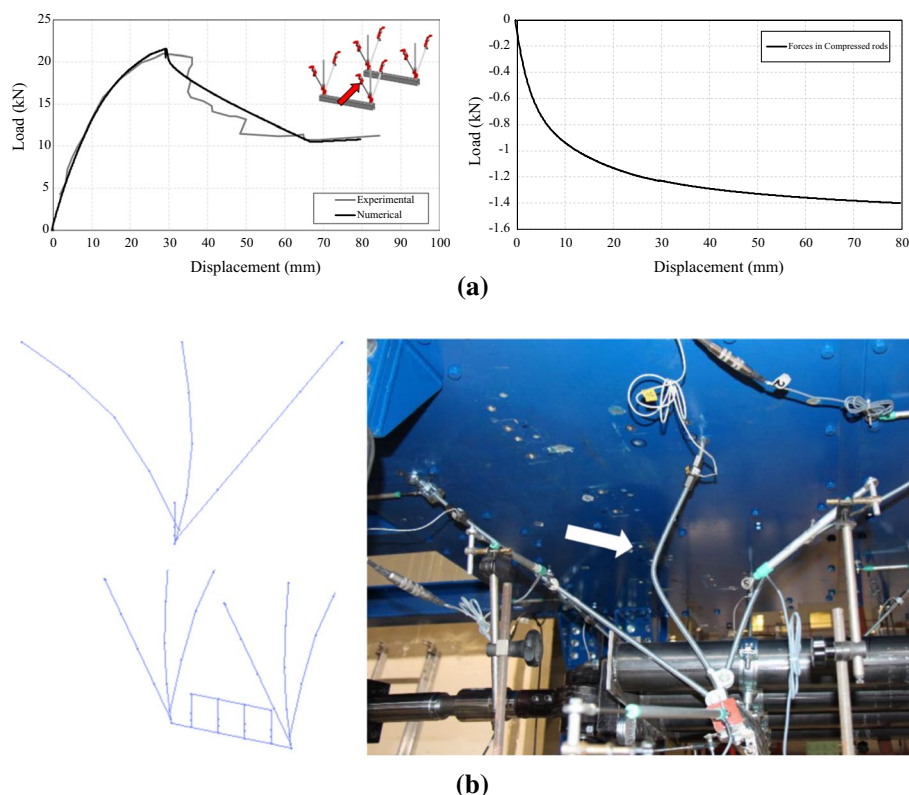


**Fig. 33** Comparison between experimental results and numerical predictions for sub-assembly SS4: **a** force–displacement response and behaviour of the rods in compression, **b** deformed shape and damage/failure mechanism

3. The effective ductility ( $\mu_{eff}$ ): defined as the ratio  $\Delta_U/\Delta_Y$ , where  $\Delta_Y$  is the effective yield displacement (defined as the ratio  $Q_M/K_I$ ) and  $\Delta_U$  is the ultimate deformation corresponding to a strength of  $0.8 Q_M$ .

These three performance parameters were extracted from the experimental and numerically-predicted hysteretic load–displacement responses of suspended piping restraint installations. These performance parameters are illustrated in Fig. 34.

Table 5 lists the performance parameters for the four sub-assemblies (SS1 to SS4) that were calculated on the basis of the FEMA P-795 (FEMA 2011) methodology using the experimental results presented by Perrone et al. (2020) and the numerical predictions obtained in this study. A very good match (differences less than 15%) is obtained in terms of maximum strength ( $Q_M$ ) and initial stiffness ( $K_I$ ). A higher mismatch is observed in terms of ductility ( $\mu_{eff}$ ) for configuration SS2 due to the reason explained above (see Fig. 31a). These results indicate that the numerical models developed in this study based on component testing can be used to determine with acceptable accuracy the performance parameters of suspended piping restraint installations without the need to conduct further sub-assembly tests.

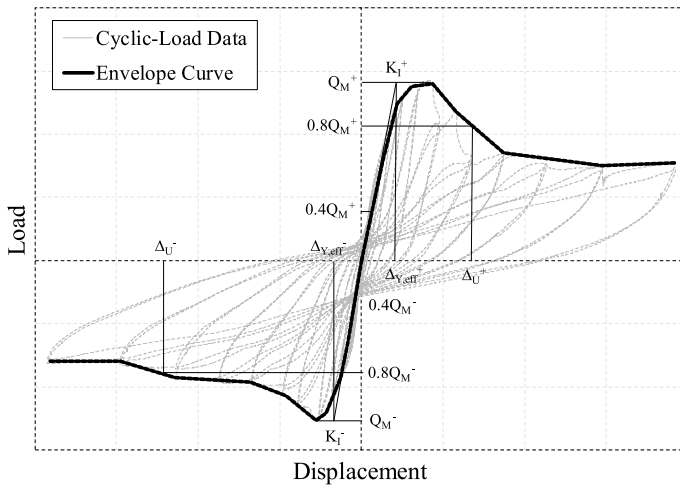


**Fig. 34** Evaluation of performance parameters (after FEMA (2011))

**Table 5** Comparison between numerical and experimental performance parameters

ID	Experimental			Numerical			Percentage difference		
	$Q_M$ (kN)	$K_I$ (kN/mm)	$\mu_{eff}$ (-)	$Q_M$ (kN)	$K_I$ (kN/mm)	$\mu_{eff}$ (-)	$Q_M$ (-)	$K_I$ (-)	$\mu_{eff}$ (-)
SS1	14.1	1.0	1.5	13.9	1.0	1.5	1.4	0.0	1.4
SS2	19.1	1.0	2.0	21.1	0.9	3.3	10.5	12.0	64.0
SS3	10.9	1.8	2.2	11.0	1.8	1.7	1.0	0.0	20.9
SS4	22.2	1.3	2.9	21.5	1.5	2.6	3.2	13.3	9.3

## 7 Conclusions

The numerical modelling of suspended piping trapeze restraint installations is described in this paper. The main objective of this study was to develop reliable numerical models of suspended piping trapeze restraint installations for the prediction of monotonic force–displacement curves from which performance parameters to be used in the performance-based seismic design framework can be extracted. Four typologies of suspended piping restraint installations were modelled: (1) trapezes with transverse channel bracing systems, (2) trapezes with longitudinal channel bracing systems, (3) trapezes with transverse rod bracing systems, and (4) trapezes with longitudinal rod bracing systems. The numerical models were developed based on cyclic test data of the components that make up suspended piping trapeze restraint installations. The prediction capabilities of the numerical models were assessed against benchmark sub-assembly test results described in a previous work. Based on the results obtained, the following main considerations can be drawn:

1. Six components were tested during the experimental program. The components were selected based on a critical evaluation of the geometrical configurations as well as on the results of the sub-assembly tests.

2. No brittle failure occurred in any of the component tests and all components exhibited ductile response.
3. Mechanics-based component models were developed for three of the tested components (i.e. pipe rings in the longitudinal direction, connection between the horizontal and vertical channel, connection of the diagonal rods to the supporting system). The component numerical models reproduced accurately the response of the tested specimens for the entire range of imposed displacements. For the components for which the numerical models were not developed, the mechanical properties were directly introduced in the sub-assembly models.
4. The numerical models developed for the channel configurations were able to reproduce relatively accurately the results of the benchmark sub-assembly tests both in terms of force–displacement curves and failure modes. The failure mode of the suspended piping trapeze restraint installation braced in the transverse direction is controlled by yielding of the connection between the diagonal and horizontal channel while in the longitudinal direction it is related to the shear failure of the pipe ring threaded rods. The numerical models were able to predict both failure modes correctly.
5. The numerical models developed for rod suspended piping trapeze restraint installations were also capable of predicting their monotonic responses accurately. The deformed shapes predicted by the numerical models reproduced accurately the buckling that occurred in the vertical and diagonal rods during the benchmark sub-assembly tests.
6. The comparison between numerically-predicted and experimental performance parameters, identified as the most critical for the elaboration of performance-based seismic design procedures for suspended piping restraint installations, demonstrated the effectiveness of the developed mechanics-based numerical models in predicting with acceptable accuracy these performance parameters without the need to conduct sub-assembly tests.

All the components and sub-assemblies considered in this study were intentionally tested beyond their ultimate limit. All these failures occurred at loads far beyond the published technical resistance data of these products.

**Acknowledgements** The numerical study described in this paper was conducted as part of a collaborative research program between Hilti Corporation and the European Centre for Training and Research in Earthquake Engineering (EUCENTRE) Foundation. The authors are grateful to Hilti Corporation for funding the experimental program. The work has been also developed within the framework of the project “Dipartimenti di Eccellenza”, funded by the Italian Ministry of University and Research at the University School for Advanced Studies IUSS Pavia.

## References

- ASCE (2017) ASCE/SEI 41-17: Seismic evaluation and retrofit of existing buildings. American Society of Civil Engineers, Structural Engineering Institute, Reston
- Blasi G, Aiello MA, Maddaloni G, Pecce MR (2018) Seismic response evaluation of medical gas and fire-protection pipelines' Tee-Joints. *Eng Struct* 173:1039–1053
- Chock G, Robertson I, Nicholson P, Brandes H, Medley E, Okubo P, Hirshorn B, Sumada J, Kindred T, Linurna G, Sarwar A, Dal Pino J, Holmes W (2006) Compilation of observations of the October 15, 2006, Kiholo Bay (Mw 6.7) and Mahukona (Mw 6.0) earthquakes, Hawaii. *Earthquake Engineering Research Institute*, Oakland, p 53
- Ercolino M, Petrone C, Coppola O, Magliulo G (2012) Report sui danni registrati a San Felice sul Panaro (Mo) in seguito agli eventi sismici del 20 e 29 maggio 2012 – v1.0. <http://www.reluis.it/>



- FEMA (2007) Interim testing protocols for determining the seismic performance characteristics of structural and nonstructural components, FEMA 461. Federal Emergency Management Agency, Washington, DC
- FEMA (2011) Quantification of building seismic performance factors: component equivalency methodology, FEMA P-795. Federal Emergency Management Agency, Washington, DC
- Filiatrault A, Uang CM, Folz B, Christopoulos C, Gatto K (2001) Reconnaissance report of the February 28, 2001 Nisqually (Seattle-Olympia) earthquake. In: Structural systems research project report no. SSRP-2000/15. Department of Structural Engineering, University of California, San Diego, La Jolla
- Filiatrault A, Perrone D, Merino R, Calvi GM (2018a) Performance-based seismic design of non-structural building elements. *J Earthq Eng*. <https://doi.org/10.1080/13632469.2018.1512910>
- Filiatrault A, Perrone D, Brunesi E, Beiter C, Piccinin R (2018b) Effect of cyclic loading protocols on the experimental seismic performance evaluation of suspended piping restraint installations. *Int J Pip Vesels* 166:61–71. <https://doi.org/10.1016/j.ijpvp.2018.08.004>
- Filippou FC, Popov EP, Bertero VV (1983) Effects of bond deterioration on hysteretic behavior of reinforced concrete joints. In: Report EERC 83-19, earthquake engineering research center. University of California, Berkeley
- Gunay S, Mosalam KM (2013) PEER performance-based earthquake engineering methodology, revisited. *J Earthq Eng* 17(6):829–858
- Gupta A, McDonald BM (2008) Performance of building structures during the October 15, 2006 Hawaii earthquake. In: Proceedings of the 14th world conference on earthquake engineering. Beijing
- McKenna F, Fenves GL, Scott MH (2006) OpenSees: open system for earthquake engineering simulation. In: Pacific Earthquake Engineering Research Center. University of California, Berkeley. <http://opensees.berkeley.edu>
- Miranda E, Mosqueda G, Retamales R, Pekcan G (2012) Performance of non-structural components during the February 27, 2010 Chile earthquake. *Earthq Spectra* 28(S1):S453–S471
- O'Reilly GJ, Perrone D, Fox M, Monteiro R, Filiatrault A (2018) Seismic assessment and loss estimation of existing school buildings in Italy. *Eng Struct* 168(1):142–162. <https://doi.org/10.1016/j.engstruct.2018.04.056>
- Perrone D, Calvi PM, Nascimbene R, Fischer E, Magliulo G (2019) Seismic performance and damage observation of non-structural elements during the 2016 Central Italy Earthquake. *Bull Earthq Eng* 17:5655–5677. <https://doi.org/10.1007/s10518-018-0361-5>
- Perrone D, Filiatrault A, Peloso S, Brunesi E, Beiter C, Piccinin R (2020) Experimental seismic performance evaluation of suspended piping trapeze restraint installations. *Bull Earthq Eng* 18:1499–1524. <https://doi.org/10.1007/s10518-019-00755-5>
- SEAOC (1995) Performance-based seismic engineering. In: SEAOC vision 2000 committee. Structural Engineers Association of California, Sacramento
- Soroushian S, Zaghi AE, Maragakis M, Echevarria A, Tian Y, Filiatrault A (2015a) Analytical seismic fragility analyses of fire sprinkler piping systems with threaded joints. *Earthq. Spectra* 31(2):1125–1155
- Soroushian S, Zaghi AE, Maragakis M, Echevarria A, Tian Y, Filiatrault A (2015b) Seismic fragility study of fire sprinkler piping systems with grooved fit joints. *J Struct Eng* 141(6):1–15
- Tian Y, Filiatrault A, Mosqueda G (2014) Experimental seismic fragility of pressurized fire suppression sprinkler piping joints. *Earthq. Spectra* 30(4):1733–1748
- Tian Y, Filiatrault A, Mosqueda G (2015a) Seismic response of pressurized fire sprinkler piping systems II: numerical study. *J. Earthq. Eng.* 19:674–699
- Tian Y, Filiatrault A, Mosqueda G (2015b) Seismic response of pressurized fire sprinkler piping systems I: experimental study. *J. Earthq. Eng.* 9:649–673
- Wood RL, Hutchinson TC, Hoehler MS, Kreidl B (2014) Experimental characterization of trapeze assemblies supporting suspended non-structural systems. In: Proceedings of the tenth U.S. National Conference on Earthquake Engineering, paper no. 905. Anchorage, Alaska